Dynamic and structural stability of cubic vanadium nitride

A. B. Mei,[1] O. Hellman,[2,3] N. Wireklint,[4] C. M. Schlepütz,[5] D. G. Sangiovanni,[2] B. Alling,[2] A. Rockett,[1] L. Hultman,[2] I. Petrov,[1,2] and J. E. Greene[1,2]

[1]*Department of Materials Science and the Materials Research Laboratory, University of Illinois, 104 South Goodwin, Urbana, Illinois 61801, USA*

[2]*Department of Physics (IFM), Linköping University, SE-58183 Linköping, Sweden*

[3]*Department of Applied Physics and Materials Science, California Institute of Technology, Pasadena, California 91125, USA*

[4]*Department of Applied Physics, Chalmers University of Technology, SE-41296 Göteborg, Sweden*

[5]*X-Ray Science Division, Advanced Photon Source, Argonne National Laboratory, 9700 S. Cass Avenue, Argonne, Illinois 60439, USA*

Structural phase transitions in epitaxial stoichiometric VN/MgO(011) thin films are investigated using temperature-dependent synchrotron x-ray diffraction (XRD), selected-area electron diffraction (SAED), resistivity measurements, high-resolution cross-sectional transmission electron microscopy, and *ab initio* molecular dynamics (AIMD). At room temperature, VN has the B1 NaCl structure. However, below $T_c = 250$ K, XRD and SAED results reveal forbidden $(00l)$ reflections of mixed parity associated with a noncentrosymmetric tetragonal structure. The intensities of the forbidden reflections increase with decreasing temperature following the scaling behavior $I \propto (T_c - T)^{1/2}$. Resistivity measurements between 300 and 4 K consist of two linear regimes resulting from different electron/phonon coupling strengths in the cubic and tetragonal-VN phases. The VN transport Eliashberg spectral function $\alpha_{\mathrm{tr}}^2 F(\hbar\omega)$, the product of the phonon density of states $F(\hbar\omega)$ and the transport electron/phonon coupling strength $\alpha_{\mathrm{tr}}^2(\hbar\omega)$, is determined and used in combination with AIMD renormalized phonon dispersion relations to show that anharmonic vibrations stabilize the NaCl structure at $T > T_c$. Free-energy contributions due to vibrational entropy, often neglected in theoretical modeling, are essential for understanding the room-temperature stability of NaCl-structure VN, and of strongly anharmonic systems in general.

I. INTRODUCTION

Group-VB transition-metal (TM) nitrides with ten valence electrons per formula unit—VN, NbN, and TaN—are known to have the B1 NaCl structure at room temperature [1–4]. However, first-principles density-functional theory (DFT) calculation results show that in the ideal B1 structure, these compounds exhibit dynamic instabilities characterized by imaginary acoustic-phonon energies around the X point at 0 K [5,6]. Physically, imaginary energies indicate that the restoring forces experienced by displaced atoms, in the presence of lattice vibrational waves, are insufficient to return atoms to their ideal positions; instead, atoms become trapped in potential energy minima located at different crystallographic coordinates, thus leading to a crystal structure transformation. Three decades ago, Kubel *et al.* [7] reported a cubic-to-tetragonal phase transition upon cooling bulk polycrystalline stoichiometric VN samples below 204 K. Lattice symmetry breaking was observed by x-ray diffraction and confirmed by heat capacity measurements. Recently, Ivashchenko *et al.* [8] found, using density-functional perturbation theory, that the low-temperature tetragonal-VN structure is dynamically stable at 0 K, with all phonon modes exhibiting positive, real energies.

A rigorous explanation of the thermodynamic stability of room-temperature stoichiometric NaCl-structure VN is lacking. Ivashchenko and Turchi [6] simulated vacancies on both cation and anion VN sublattices by convolving the ideal VN band structure with Gaussian functions. They linked increases in the electronic temperature, i.e., broadening of convoluted linewidths, to increased vacancy concentrations and found that the cubic-VN structure becomes energetically favored over the tetragonal structure at absolute zero when the joint vacancy concentration is greater than 6% on both sublattices. Weber *et al.* [9] determined room-temperature phonon dispersion relations for bulk understoichiometric single-crystal $VN_{0.86}$ using inelastic neutron scattering and showed that, in the presence of anion vacancies, acoustic-phonon energies around the X point are real, thus reflecting a dynamically stable cubic structure. Kubel *et al.* [7] reported that polycrystalline understoichiometric bulk VN_{1-x} samples with $x > 0.03$ remain in the cubic phase when cooled to cryogenic temperatures and do not undergo the cubic-to-tetragonal phase transition observed in their stoichiometric samples.

We have previously shown that high-structural-quality single-crystal stoichiometric VN/MgO(011) films have the NaCl structure [10]. Thus, vacancies are not necessary to stabilize the cubic phase. Instead, we show here that cubic VN is dynamically stabilized by anharmonic atomic vibrations.

We use temperature-dependent synchrotron x-ray diffraction (XRD), high-resolution cross-sectional transmission electron microscopy (HR-XTEM), selected-area electron diffraction (SAED), *ab initio* molecular dynamics (AIMD), and resistivity ρ measurements to investigate structural phase transitions in stoichiometric VN/MgO(011) thin films. Between 300 and 250 K, XRD scans and SAED patterns consist only of single-crystal reflections with Miller indices which are all even or all odd, consistent with the NaCl-structure factor. At lower temperatures, we observe forbidden reflections with Miller indices of mixed parity associated with a tetragonal-VN phase. The intensities I of the forbidden reflections increase upon cooling below $T_c = 250$ K following the scaling relationship $I \propto (T_c - T)^{1/2}$. Temperature-dependent resistivity measurements show that $\rho(T)$ contains two linear regions, at $250 \lesssim T \lesssim 300$ K and $100 \lesssim T \lesssim 150$ K, the latter due to

stronger electron/phonon interactions in the tetragonal versus cubic phase.

Computational endeavors aimed at predicting the stability of crystal phases often neglect vibrational entropies and rely solely on internal energies. In most crystal systems, this assumption is justified since differences in crystal vibrational entropies are relatively small compared to differences in crystal potential energies [11,12]. As a result, the difference in the Gibbs free energies ΔG—the thermodynamic quantity governing phase stability—between the competing phases is, at zero pressure, to a very good approximation, simply the difference in their internal energies. For VN, however, we show in the present work that the inclusion of anharmonic lattice vibrations and vibrational entropy is essential in order to explain structural stability.

Using AIMD within the framework of the temperature-dependent effective potential method [13,14], we calculate renormalized phonon dispersion relations (including many-body and self-interactions) for NaCl-structure VN as a function of temperature between 400 and 200 K. The results show cubic VN to be dynamically stable above $T_c = 250$ K due to anharmonic effects, with all phonon branches exhibiting real energies. As the temperature is decreased, acoustic-phonon softening occurs around the X point, consistent with a transition to the tetragonal structure. From temperature-dependent resistivity measurements, we obtain, through an Einstein inversion procedure [15], the VN Eliashberg spectral function $\alpha_{\mathrm{tr}}^2 F(\hbar\omega)$, a measure of the phonon density of states $F(\hbar\omega)$ weighted by the electron/phonon interaction strengths $\alpha_{\mathrm{tr}}^2(\hbar\omega)$. Spectral features corresponding to acoustic phonons are observed at $\hbar\omega = 25$ meV in the tetragonal-VN phase, significantly higher than the value $\hbar\omega = 19$ meV obtained by room-temperature neutron-scattering measurements carried out on bulk NaCl-structure VN. Together with results from anharmonic perturbation theory, the lower phonon energies of the cubic-VN phase yield higher vibrational entropies which, at $T > T_c$, stabilize the cubic structure compared to the tetragonal phase, the thermodynamic ground state at absolute zero. The results testify to the importance of including many-body renormalization effects and vibrational entropies when describing the stability of material systems characterized by large anharmonicity at elevated temperatures.

II. EXPERIMENTAL PROCEDURE

Single-crystal, 300-nm-thick, stoichiometric B1 NaCl-structure VN layers are grown epitaxially on $10 \times 10 \times 0.5$ mm^3 MgO(011) substrates in pure N_2 atmospheres at $T_s = 430$ °C in a load-locked ultrahigh-vacuum magnetically unbalanced stainless-steel dc reactive magnetron sputter-deposition system described in Ref. [16]. The system base pressure is 5×10^{-10} Torr (7×10^{-8} Pa). Ultrahigh purity (99.9999%) N_2 is introduced through high-precision solenoid valves; the pressure is measured by a capacitance manometer and maintained constant at $P_{N_2} = 20$ mTorr (2.67 Pa) using an automatic mass-flow controller. The power applied to the 76-mm-diameter V target (purity 99.95%) is 100 W (467 V and 0.222 A), yielding a VN deposition rate of 0.1 nm/s.

Prior to growth, polished MgO(011) substrates are cleaned and degreased by successive rinses in ultrasonic baths of trichloroethane, acetone, methanol, and deionized water, and blown dry in dry N_2. The substrates are then mounted on resistively heated Ta platens using Mo clips and inserted into the sample introduction chamber for transport to the growth chamber where they are thermally degassed at 800 °C for 1 h [17].

Composition and structure of as-deposited samples are determined using a combination of Rutherford backscattering spectrometry (RBS), high-resolution x-ray diffraction (HR-XRD), HR-XTEM, and SAED. The RBS probe beam consists of 2 MeV He$^+$ ions, incident at 22.5° relative to the sample surface normal, with a total accumulated ion dose of 100 μC; the detector is set at a 150° scattering angle. Backscattered spectra are analyzed using the SIMNRA simulation program [18] yielding N/V ratios of 1.00 ± 0.03.

HR-XTEM images and SAED patterns are acquired in a JEOL 2100 transmission electron microscope equipped with a LaB$_6$ crystal field-emission source operated at 200 keV. Cross-sectional specimens are prepared by gluing films to glass slides and cutting vertical sections. The samples are mechanically ground to thicknesses of $\simeq 30$ μm and then thinned to electron transparency using a Gatan PIPS ion miller with two 3.5 keV Ar$^+$ beams incident simultaneously from above and below the substrate at shallow angles of 8°. Samples are rotated during ion etching. Final thinning is carried out using 100 eV Ar$^+$ ions.

XRD θ-2θ scans are acquired in a Philips Xpert MRD diffractometer using Cu $K\alpha$ radiation (wavelength $\lambda = 0.154\,18$ nm) in line focus. The primary optics on the diffractometer consist of a parabolic mirror and a two-reflection Ge monochromator, providing an angular beam divergence of <12 arc sec with a wavelength spread of $\Delta\lambda/\lambda = 7 \times 10^{-5}$; a high-speed linear detector serves as the secondary optics.

XRD pole figures, high-resolution reciprocal-space maps (HR-RSM), and scans along high-symmetry directions are obtained at beamline 33-BM of the Advanced Photon Source, Argonne National Laboratory. Experiments are performed with the storage ring operating in top-up mode with an electron energy of 7 GeV and an injection current of 100 mA. Using a double-crystal Si(111) monochromator, the wavelength of the x-ray probe beam is set to 0.08257 nm (15 keV). VN/MgO(011) samples, 5×5 mm^2, are mounted on a Cu cold finger, enclosed in a Be-dome-covered cryostat, and evacuated to 1×10^{-6} Torr (1.3×10^{-4} Pa). Sample temperatures are monitored using a Lake Shore Si diode thermometer and adjusted between 300 and 20 K by Joule heating. The x-ray probe beam is focused onto the detector plane, yielding 1×10^{12} photons/s incident on an 800×400 μm^2 area of the sample surface.

Temperature-dependent VN resistivities between 300 and 4 K are obtained using a Quantum Design physical property measurement system. Ohmic contacts are fabricated by Ga$^+$-ion etching, in a FEI Strata DB-235 focused ion-beam system, four 2-μm-diameter holes in the van der Pauw geometry [19], and then filling the holes with Pt without air exposure. All contacts are tested for Ohmic behavior. Current and voltage measurements are iterated through different contact pairs to account for geometric effects.

III. THEORETICAL PROCEDURE

Temperature-dependent VN phonon dispersion relations are determined from AIMD simulations using the temperature-dependent effective potential technique (TDEP). The method is described in detail in Refs. [13,14]. Briefly, anharmonic atomic displacement $\mathbf{u}_j$ and forces $\mathbf{F}_i$ are obtained from AIMD simulations carried out at finite temperatures and used together with Hooke's law to obtain temperature-dependent effective interatomic force constant matrices $\mathbf{\Phi}_{ij}$ which obey cubic symmetry and best reproduce the anharmonic behavior; that is, which minimize $\Delta F = \sum_{t,i} |\mathbf{F}_i - \sum_j \mathbf{\Phi}_{ij}\mathbf{u}_j|$ for all AIMD time steps t. Indices i and j refer to crystallographic directions. By interpolating the finite-temperature set, together with results obtained at absolute zero, of symmetry-irreducible [13] effective force constant matrices $\mathbf{\Phi}_{ij}$, force constant matrices $\widetilde{\mathbf{\Phi}}_{ij}$ at arbitrary temperatures are determined. From the Fourier transformed $\widetilde{\mathbf{\Phi}}_{ij}$ matrices, dynamical matrices $\mathbf{D}_{ij}$ are obtained and diagonalized to yield the temperature-dependent VN phonon dispersion relations.

Atomic forces $\mathbf{F}$ are computed at each molecular dynamics time step from self-consistent electronic charge densities $n[r]$ using the Hellmann-Feynman theorem [20,21]. The required $n[r]$ values are obtained within the density-functional theory framework by self-consistently solving the Kohn-Sham equations [22] using the projector augmented wave method [23] as implemented in VASP [24–26]. VN is modeled as a supercell consisting of five repetitions of the B1 unit cell in each Cartesian direction ($5 \times 5 \times 5$), corresponding to 250 atoms. V pseudopotentials are based on s and d valence states; N pseudopotentials are based on s and p states. Electronic exchange and correlation effects are parametrized using the AM05 functional [27] and the plane wave expansion is carried out up to a cut-off energy of 500 eV. Brillouin-zone integration is performed using the Γ point. Temperature-dependent effective force constant matrices $\mathbf{\Phi}_{ij}$ are obtained from AIMD simulations at $T = 300, 600, 900,$ and 1200 K. Thermal expansion effects are treated by minimizing, at each temperature, the Helmholtz free energy as a function of volume using a parabolic fit; for this purpose, simulations are carried out using five supercell volumes based on lattice parameters 0.98, 0.99, 1.00, 1.01, and 1.02% of the equilibrium value at absolute zero. Simulations are run for approximately 16 000 2-fs time steps; temperature is controlled using a Nosé thermostat [28].

VN residual resistivities ρ_o due to the joint presence of cation and anion vacancies are estimated from first-principles electronic Green's function calculations using the Kubo-Greenwood formalism [29–34]. The calculations are based on the primitive face-centered-cubic unit cell with a two-atom basis set and the experimental VN lattice parameter value $a_o = 0.4132$ nm. Vacancy-induced disorder is modeled within the coherent-potential approximation [35]. Expansion of the electronic wave function in terms of atomic s, p, and d spherical harmonics is performed using the atomic-sphere approximation with equal, chemistry-independent, sphere radii; we find *a posteriori* that this configuration yields the smallest ρ_o value and, thus, the highest, most conservative, estimate of the vacancy density [36]. Self-consistent VN electronic Green's functions are solved using the Korringa-
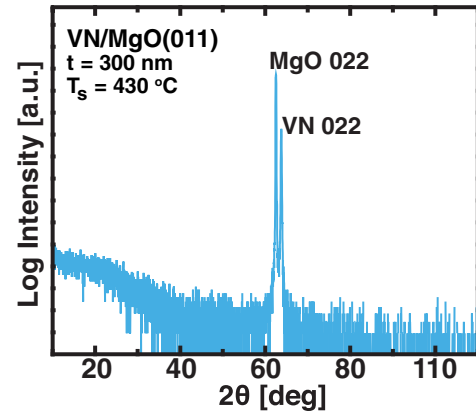

FIG. 1. (Color online) θ-2θ XRD scan, acquired using Cu $K\alpha$ radiation, from a 300-nm-thick epitaxial VN/MgO(011) layer grown at $T_s = 430\,°\text{C}$ by reactive magnetron sputter deposition.

Kohn-Rostoker approximation [37,38] as implemented in SPR-KKR [32–34]. Electron exchange and correlation effects are treated within the generalized gradient approximation as parametrized by Perdew, Burke, and Ernzerhof [39]. Resulting VN electronic band dispersion relations are found to be in good agreement with those computed independently with VASP.

IV. RESULTS AND DISCUSSION

A. VN/MgO(011) film stoichiometry and nanostructure

RBS results establish that the VN/MgO(011) layers are stoichiometric, and compositionally uniform, with N/V = 1.00 ± 0.03. Combined with XTEM measurements of film thickness, RBS-determined atomic areal densities yield a VN mass density of 6.1 g/cm^3, equal to reported results for bulk crystals [40].

A typical XRD θ-2θ scan, acquired using Cu $K\alpha$ radiation, from a VN/MgO(011) film is shown in Fig. 1; diffracted x-ray intensities are plotted logarithmically as a function of 2θ between 10° and 110°. Over the entire 2θ range sampled, the scan exhibits only one pair of reflections, with peaks at 62.29 and 63.59° 2θ assigned to MgO 022 and VN 022.

Figures 2(a) and 2(b) are typical synchrotron x-ray diffraction {111} pole figures obtained from VN/MgO(011) samples. The pole figures are plotted as stereographic projections over azimuthal angles $\varphi = 0°-360°$ and polar angles $\chi = 0°-85°$ with diffracted intensities represented by logarithmic isointensity contours. The {111} VN(011) pole figure in Fig. 2(a) exhibits two peaks, separated by $\varphi = 180°$ and tilted $\chi = 35.26°$ from the surface normal, corresponding to the 111 and $\bar{1}$11 reflections of a cubic structure. No additional reflections are observed. The {111} pole figure from MgO(011) contains a pair of reflections positioned at φ and χ angles identical to those observed for VN(011), showing that $[111]_{VN}||[111]_{MgO}$. VN(011) and MgO(011) {002} pole figures, presented in Fig. 2(b), also exhibit two peaks each, located, in this case, at $\varphi = 0°$ and 180° with $\chi = 45°$, corresponding to 002 and 020 cubic reflections.

A typical VN/MgO(011) HR-XTEM image, acquired along the $0\bar{1}1$ zone axis, is shown in Fig. 3. Image contrast between the film and substrate arises predominantly from
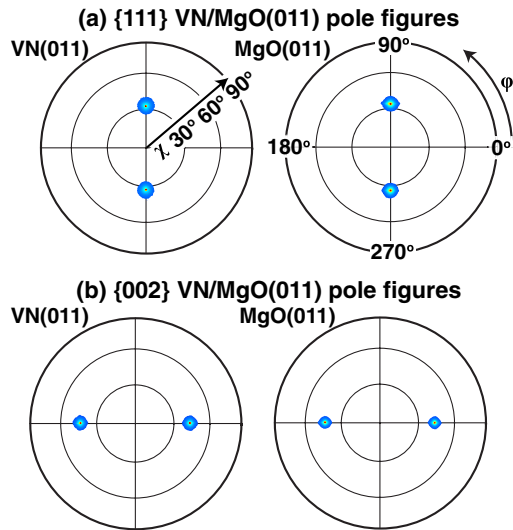
FIG. 2. (Color online) Synchrotron x-ray diffraction VN and MgO (a) {111} and (b) {002} pole figures acquired from 300-nm-thick epitaxial VN/MgO(011) layers grown at $T_s = 430\,^\circ$C by reactive magnetron sputter deposition.

the large difference in mass between V ($m_{\rm V} = 50.9$ amu) and Mg ($m_{\rm Mg} = 24.3$ amu). Based upon the combination of x-ray $\theta-2\theta$ and pole figure measurements, together with the observation of well-ordered 001, 011, and 111 lattice fringes across the film-substrate interface, we establish that the VN films are single crystals which are epitaxially oriented cube-on-cube with respect to their MgO substrates: $(011)_{\rm VN}||(011)_{\rm MgO}$ with $[100]_{\rm VN}||[100]_{\rm MgO}$. Film and substrate lattice parameters obtained from the fringe spacings are 0.413 and 0.421 nm, respectively.

Figure 4 is an x-ray diffraction HR-RSM, acquired using Cu $K\alpha$ radiation, around the 022 film and substrate reflections and plotted as logarithmic isointensity contours as a function of in-plane $k_{||}$ and out-of-plane $k_\perp$ reciprocal-lattice vectors. Peak positions in reciprocal space are related to those in ω-2θ space
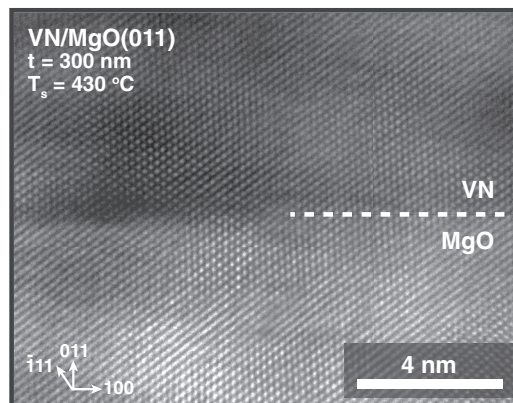

FIG. 3. High-resolution cross-sectional TEM image acquired along the [$0\bar{1}\bar{1}$] zone axis from a 300-nm-thick epitaxial VN layer grown on MgO(011) at $T_s = 430\,^\circ$C by reactive magnetron sputter deposition.
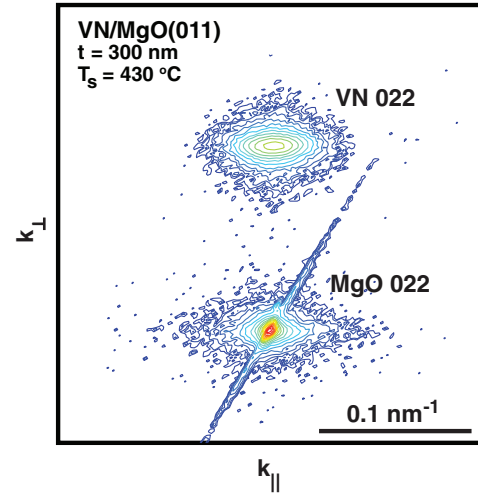

FIG. 4. (Color online) High-resolution reciprocal-space x-ray diffraction map, acquired with Cu $K\alpha$ radiation, about the symmetric 022 reflection from a 300-nm-thick epitaxial VN layer grown on MgO(011) at $T_s = 430\,^\circ$C by reactive magnetron sputter deposition.

via $k_{||} = 2r_{\rm E}\sin(\theta)\cos(\omega - \theta)$ and $k_\perp = 2r_{\rm E}\sin(\theta)\sin(\omega - \theta)$ in which $r_{\rm E}$ is the radius of the Ewald sphere [41,42].

VN(011) in-plane $\xi_{||}$ and out-of-plane $\xi_\perp$ x-ray coherence lengths, which serve as measures of crystalline quality, are obtained from the width of symmetric 022 reflections parallel $\Delta k_{||}$ and perpendicular $\Delta k_\perp$ to the diffraction vector k through the relationships: $\xi_{||} = 2\pi/|\Delta k_{||}|$ and $\xi_\perp = 2\pi/|\Delta k_\perp|$. From the results shown in Fig. 4, $\xi_{||} = 59$ and $\xi_\perp = 140$ nm. For comparison, high-structural-quality single-crystal ZrN/MgO(001) films, 830 nm thick (nearly $3\times$ thicker than the present VN film), grown under similar conditions exhibit $\xi_{||} = 18$ and $\xi_\perp = 161$ nm [43]. Out-of-plane $\xi_\perp$ values depend, in addition to structural quality, on film thickness. The relatively large ξ values obtained here, comparable to well-ordered 300-nm-thick VN(001), $\xi_{||} = 57$ and $\xi_\perp = 159$ nm [10], and 260-nm-thick TiN(001), $\xi_{||} = 86$ and $\xi_\perp = 142$ nm [42], reflect the high crystalline quality and low mosaicity of our films.

In-plane $a_{||}$, out-of-plane $a_\perp$, and relaxed a_o VN lattice parameters are determined, together with in-plane $\varepsilon_{||}$ and out-of-plane $\varepsilon_\perp$ film strains, from HR-RSMs about asymmetric 311 reflections. Typical HR-RSM results are shown in Fig. 5 as logarithmic isointensity contours plotted vs $k_{||}$ and $k_\perp$ reciprocal-lattice vectors. For a 311 reflection from a 011-oriented NaCl-structure sample, the in-plane $a_{||}$ and out-of-plane $a_\perp$ lattice parameters are related to the reciprocal-lattice vectors through the relations $a_{||} = 3/k_{||}$ and $a_\perp = \sqrt{2}/k_\perp$ [10]. From measured $k_{||}$ and $k_\perp$ values, we obtain $a_{||} = 0.4124$ and $a_\perp = 0.4136$ nm. Combining these results with the VN Poisson ratio $\nu = 0.19$ [10], the relaxed VN lattice parameter is determined via the equation [44]

$$a_o = \frac{a_\perp(1-\nu) + a_{||}(2\nu)}{(1+\nu)}, \qquad (1)$$

as $a_o = 0.4132 \pm 0.0004$ nm. The result is in agreement with the HR-XTEM results and with published values for bulk VN, 0.4134 nm [45,46]. The mild in-plane compressive strain,
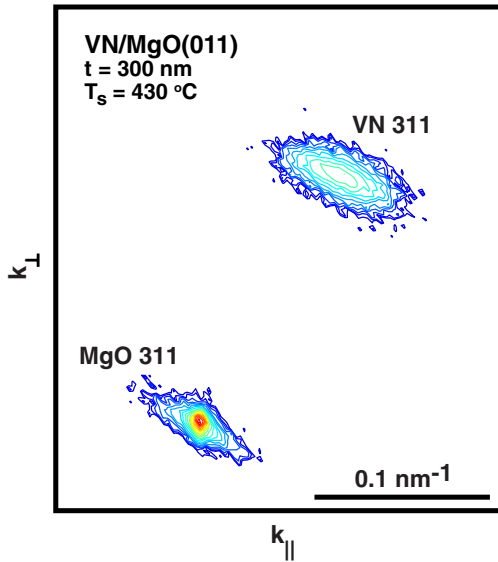
FIG. 5. (Color online) High-resolution reciprocal-space x-ray diffraction map, acquired with Cu $K\alpha$ radiation, about an asymmetric 311 reflection from a 300-nm-thick epitaxial VN layer grown on MgO(011) at $T_s = 430\,°C$ by reactive magnetron sputter deposition.

$\varepsilon_{\parallel} = (a_{\parallel}/a_o - 1) = -0.0019$, is primarily accounted for by differential thermal contraction during cooling following film deposition. Using the thermal contraction coefficients for MgO, $\alpha_s = 13 \times 10^{-6}\,\mathrm{K}^{-1}$ [47], and VN, $\alpha_f = 9.7 \times 10^{-6}\,\mathrm{K}^{-1}$ [48], we obtain a thermal strain of $\varepsilon_{\parallel} = -0.0017$. Film out-of-plane strain $\varepsilon_{\perp} = (a_{\perp}/a_o - 1) = 0.0010$.

B. Temperature-dependent electron and synchrotron x-ray diffraction

The thermal stability of stoichiometric VN in the NaCl structure is probed by temperature-dependent SAED, synchrotron x-ray diffraction, and resistivity measurements $\rho(T)$. SAED patterns are acquired at 300, 263, 258, 248, 228, 173, 148, 133, and 97 K. Figure 6(a) is a typical room-temperature SAED pattern obtained along the $0\bar{1}1$ zone axis with the selected-area aperture sampling the upper 200-nm portion of the film. Only single-crystal reflections are visible, consistent
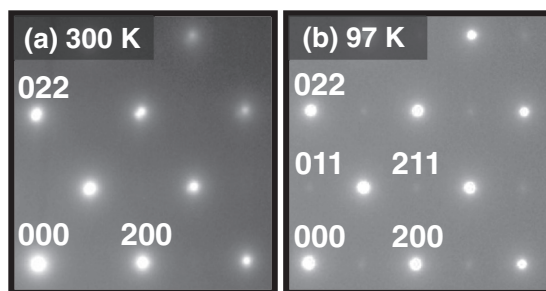

FIG. 6. Typical temperature-dependent selected-area electron diffraction patterns, acquired along the [0$\bar{1}$1] zone axis, from epitaxial stoichiometric VN/MgO(011) at (a) room temperature and (b) 97 K with the selected-area aperture sampling the upper 200 nm of the film. The VN(011) film was grown at $T_s = 430\,°C$ by reactive magnetron sputter deposition.
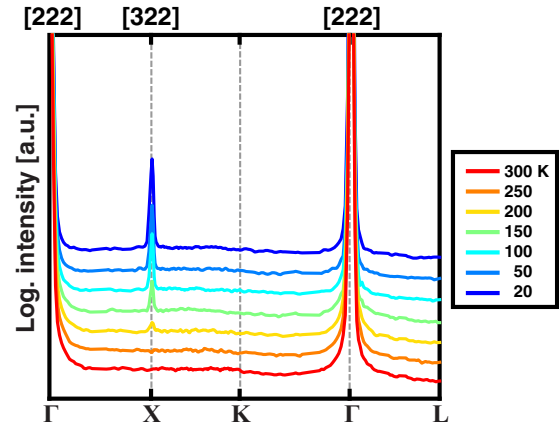

FIG. 7. (Color online) Temperature-dependent synchrotron x-ray diffraction intensities, acquired along high-symmetry reciprocal-space directions, from a 300-nm-thick epitaxial VN/MgO(011) layer grown at $T_s = 450\,°C$. Γ, X, K, and L points correspond to [222], [322], [2.75 2.75 2], [222], and [2.5 2.5 2.5] positions in reciprocal [hkl] space.

with synchrotron x-ray diffraction pole figures [Figs. 2(a) and 2(b)], HR-XTEM observation of continuous lattice fringes across the film-substrate interface (Fig. 3), and the relatively large x-ray coherence lengths obtained from HR-RSM results (Fig. 4). All SAED patterns obtained at $T < 250$ K, exhibit additional forbidden reflections associated with Miller indices of mixed parity, including 001, 003, and 211, due to a structural transition to a noncentrosymmetric tetragonal phase. Figure 6(b), acquired at 97 K, is a typical example.

The intensities of VN(011) forbidden reflections are obtained as a function of temperature from synchrotron XRD scans along high-symmetry reciprocal-space directions and HR-RSMs acquired over the temperature range from 300 to 20 K. In NaCl-structure crystals, reciprocal-lattice positions described by integer Miller indices of the same parity correspond to the [000] Γ-point Brillouin-zone center, while positions described by integer Miller indices of mixed parity correspond to the [100] X-point Brillouin-zone boundary. L-point [½½½] Brillouin-zone boundaries are represented by half-integer indices. Diffracted intensities are acquired along high-symmetry directions in the Brillouin zone, centered about the 222 Bragg reflection, and plotted logarithmically as a function of temperature in Fig. 7. The curves are displaced vertically for clarity. At room temperature, Bragg conditions are satisfied only at the Brillouin-zone center. Below 250 K, however, additional reflections, in agreement with the low-temperature SAED results in Fig. 6, appear at the X point. The intensities of the forbidden peaks increase with decreasing temperature.

VN/MgO(011) synchrotron HR-RSMs about forbidden 003 VN reflections are acquired at temperatures between 300 and 20 K. Typical maps plotted as diffracted intensity isocontours as a function of [100] and [010] reciprocal-lattice vectors k are presented in Figs. 8(a)–8(d) for $T = 275, 250, 200,$ and 100 K. Diffracted intensities are normalized at each temperature to highlight the absence of a peak at $T = 275$ K and the presence of a small 003 Bragg reflection
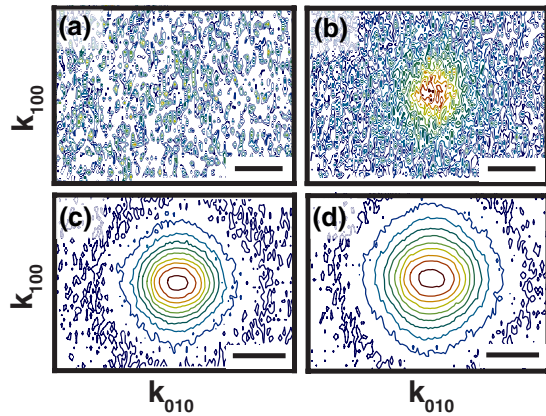
FIG. 8. (Color online) Typical temperature-dependent high-resolution reciprocal-space synchrotron x-ray diffraction maps, plotted as a function of reciprocal-lattice vectors k_{100} and k_{010}, about the asymmetric 003 reflection from a 300-nm-thick epitaxial stoichiometric VN/MgO(011) layer grown at $T_s = 430\,°C$. The maps are acquired at temperatures of (a) 275, (b) 250, (c) 200, and (d) 100 K. Scale bars correspond to $0.05\,\mathrm{nm}^{-1}$.

at $T = 250$ K. Maps at temperatures below 200 K [Figs. 8(c) and 8(d)] show well-defined 003 reflections, characterized by asymmetric isointensity contours which extend farther along [100] than [011] directions. Additional 003 RSMs (not shown) acquired from 300-nm-thick VN overlayers grown on MgO(001) and MgO(111) also exhibit forbidden reflections with mixed-parity indices which appear at temperatures below $T_c = 250$ K, indicating that the phase transition is not controlled by the film/substrate epitaxial orientation. This is in contrast to the neighboring Group-VIB compound CrN, for which 140-nm-thick films grown on MgO(001) have been shown to suppress the cubic-to-orthorhombic transition observed in bulk CrN at 280 K [49].

The temperature-dependent evolution of 003 VN reflection intensities $I(T)$ is obtained by integrating three-dimensional HR-RSM peaks acquired at temperatures between 300 and 20 K; the resulting $I(T)$ values are plotted in Fig. 9. Over the
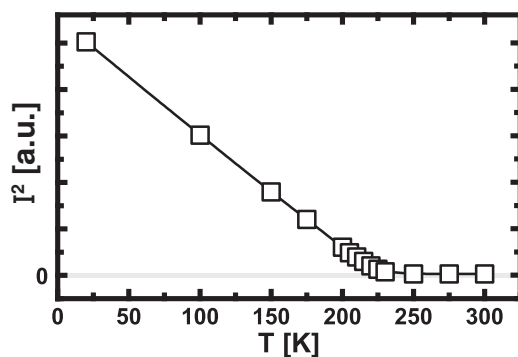

FIG. 9. Synchrotron XRD VN(011) forbidden 003 reflection intensities squared, plotted as a function of temperature. Data points correspond to integrated 003 VN peak intensities obtained from HR-RSM measurements carried out on 300-nm-thick epitaxial stoichiometric VN/MgO(011) layers, including those shown in Fig. 8.

temperature range $250 \leqslant T \leqslant 300$ K, the B1 cubic structure factor is zero. Below the transition temperature $T_c = 250$ K, $I(T)$ values increase with decreasing T, following a scaling relationship $I(T) \propto (T_c - T)^{1/2}$.

Based on the phenomenological Landau formalism for displacive structural phase transitions, a temperature scaling exponent of ½, as observed here, suggests that the phase transition is second order [50]. However, first-order phase transitions can also exhibit a critical exponent of ½ [51,52]. In that case, $I(T)$ discontinuously becomes zero at a temperature T_c^* prior to reaching T_c. The magnitude of the difference $|T_c^* - T_c|$ is a measure of the degree to which the phase transition is second order [53]. For VN, $I(T)$ appears to decrease continuously toward zero (see Fig. 9), indicating that the phase transition exhibits strong second-order character with $T_c^* \simeq T_c$. However, a second-order phase transition is forbidden by the incompatible symmetries of the VN parent cubic phase (space group $Fm\bar{3}m$) and product tetragonal ($P\bar{4}2m$) phase [7]. As a result, a discontinuous jump in $I(T)$, while below experimental detection limits, must occur at T_c^* near T_c. Thus, the cubic-to-tetragonal-VN phase transition exhibits an apparent second-order character, but ultimately requires, due to the symmetries of the parent and product phases, a discontinuous change in $I(T)$ and is therefore first order.

C. *Ab initio* molecular dynamics

Forbidden reflections of mixed parity, including 003 and 211, correspond to scattering vectors k with crystal momenta translationally symmetric to the [001] X point in the first Brillouin zone. At room temperature, inelastic neutron-scattering measurements carried out on bulk VN samples reveal phonon anomalies characterized by soft longitudinal phonon modes near the X point [9]. Quasiharmonic DFT calculations [5] show that the anomalies become pronounced at 0 K, with phonons exhibiting imaginary energies. Phonons are quantized lattice waves with amplitudes which depend on time t through the factor $\exp(-i\omega t)$ [54], in which ω is the phonon frequency. For positive phonon energies $\hbar\omega$, the lattice wave propagates with a group velocity $v_g = \nabla_k \omega$. At zero phonon energy, the wave ceases to evolve with time and the atoms are frozen at their displaced coordinates, resulting in a transformed structure. Imaginary phonon energies correspond to a wave amplitude which grows increasingly large in an unphysical manner as time progresses. This is the signature of a dynamically unstable system. In order to investigate the dynamic stability of VN, as influenced by phonon softening, temperature-dependent renormalized (including many-body and self-interactions) VN phonon dispersion relations are computed using TDEP.

Figure 10 shows calculated VN phonon dispersion relations $\hbar\omega_j(k)$ along high-symmetry directions for eight temperatures between 400 and 200 K. At 400 K, VN phonon energies are real over the entire Brillouin zone as a direct result of anharmonic vibrations. Pronounced anomalies, characterized by soft longitudinal and transverse acoustic (LA and TA) phonon modes ($\hbar\omega_{LA} = 8.7$ and $\hbar\omega_{TA} = 12.4$ meV), occur near the X point. At lower temperatures, the LA modes soften further due to attenuation of anharmonic atomic vibrations resulting from
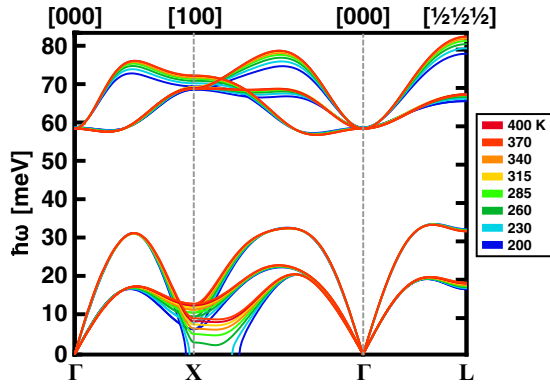
FIG. 10. (Color online) Renormalized VN phonon dispersion relations, at temperatures between 400 and 200 K, obtained using *ab initio* molecular dynamics with temperature-dependent effective potentials.
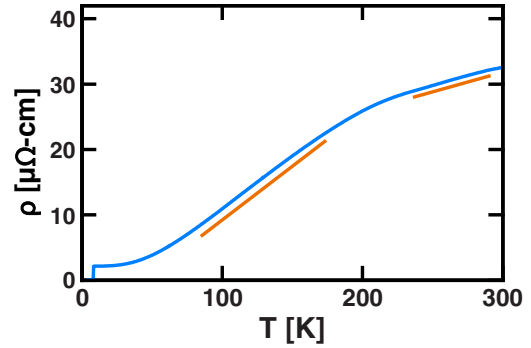

FIG. 11. (Color online) Temperature-dependent $(4 < T < 300\,\mathrm{K})$ resistivity $\rho(T)$ of epitaxial stoichiometric VN/MgO(011). Orange lines highlight the regions $250 \lesssim T \lesssim 300\,\mathrm{K}$ and $100 \lesssim T \lesssim 150\,\mathrm{K}$ for which $\rho \propto T$.

changes in the interatomic force constants and the potential energy landscape. The energy of [001]-zone-boundary LA phonons reaches zero at the critical temperature $T_c = 250\,\mathrm{K}$. Below T_c, $\hbar\omega_{\mathrm{LA}}$ becomes imaginary $(\hbar\omega_{\mathrm{LA}}{}^2 < 0\,\mathrm{meV})$. As a result, our TDEP simulations show that NaCl-structure VN becomes dynamically unstable below $T_c = 250\,\mathrm{K}$, consistent with the structural transformation observed by temperature-dependent synchrotron XRD and SAED analyses.

D. VN temperature-dependent resistivity

The acoustic-phonon density of states for the VN tetragonal phase is evaluated via the transport Eliashberg spectral function $\alpha_{\mathrm{tr}}^2 F(\hbar\omega)$, an energy-resolved measure of the product of the electron/phonon coupling strength $\alpha_{\mathrm{tr}}^2(\hbar\omega)$ and the phonon density of states $F(\hbar\omega)$. For group-IVB nitrides, the transport electron/phonon coupling function $\alpha_{\mathrm{tr}}^2(\hbar\omega)$ is essentially constant as a function of energy [15]. Similarly, for the group-VB nitride NbN, the phonon density of states, obtained by inelastic neutron-scattering measurements using bulk single crystals, exhibits peaks due to acoustic and optical phonons at $\hbar\omega_{\mathrm{A}} = 25$ and $\hbar\omega_{\mathrm{O}} = 65\,\mathrm{meV}$ [55], in good agreement with values obtained by Raman spectroscopy, $\hbar\omega_{\mathrm{A}} = 25$ and $\hbar\omega_{\mathrm{O}} = 67\,\mathrm{meV}$ [56]. Since features in Raman spectroscopy are strongly influenced by electron/phonon interactions [57–63], we conclude that in both group-IVB and VB nitrides, $\alpha_{\mathrm{tr}}^2 F(\hbar\omega)$ effectively samples the phonon density of states, allowing the energies of features in $F(\hbar\omega)$ to be obtained from temperature-dependent resistivity measurements.

The VN/MgO(011) room-temperature resistivity, $\rho_{300\,\mathrm{K}} = 33.0\,\mu\Omega\,\mathrm{cm}$, is lower than reported results for polycrystalline bulk VN, $85\,\mu\Omega\,\mathrm{cm}$ [40], and VN thin films, 34–$57\,\mu\Omega\,\mathrm{cm}$ [64–67]. Measured temperature-dependent VN/MgO(011) resistivities $\rho(T)$ between 300 and 4 K are presented in Fig. 11. Upon cooling, $\rho(T)$ decreases, due to decreased phonon scattering, with $\rho(T) \propto T$ between 300 and $\sim$250 K. The temperature coefficient of resistivity (TCR) over this temperature range, defined as $(\rho_{300\,\mathrm{K}} - \rho_{250\,\mathrm{K}})/\Delta T$, is $6.4 \times 10^{-8}\,\Omega\,\mathrm{cm}\,\mathrm{K}^{-1}$, remarkably similar to those of the group-IVB TM nitrides, which range from

4.0×10^{-8} (HfN) [68] to 5.0×10^{-8} (TiN) [15] to $5.6 \times 10^{-8}\,\Omega\,\mathrm{cm}\,\mathrm{K}^{-1}$ (ZrN) [43].

While the resistivity of group-IVB nitrides follows a linear scaling relation $\rho(T) \propto T$ over a broad temperature range spanning $100 \leqslant T \leqslant 300\,\mathrm{K}$ [15], the slope of ρ vs T for group-VB VN changes as T is decreased below 250 K. At temperatures between $\sim$150 and 100 K, the VN resistivity decreases linearly at a rate approximately three times larger, resulting in TCR $= 17 \times 10^{-8}\,\Omega\,\mathrm{cm}\,\mathrm{K}^{-1}$, than that over the temperature range 300–250 K. Thus, the VN resistivity between 300 and 100 K consists of two linear regions, $250 \lesssim T \lesssim 300\,\mathrm{K}$ and $100 \lesssim T \lesssim 150\,\mathrm{K}$, as highlighted in Fig. 11.

It has been proposed that the temperature-dependent resistivity of VN exhibits saturation [67,69], a sublinear decrease in resistivity with decreasing temperature, as is typical of A15-structure compounds [70–72] for which strong electron/phonon scattering reduces electron mean free paths to lengths comparable to interatomic spacings [73]. However, for VN, the temperature below which the slope $d\rho/dT$ decreases more rapidly coincides with the cubic-to-tetragonal phase-transition temperature $(T_c = 250\,\mathrm{K})$ determined by temperature-dependent SAED (Fig. 6) and synchrotron XRD (Figs. 7 and 8). As a result, we do not observe a sublinear VN $\rho(T)$ behavior; rather, $\rho(T)$ consists of two linear segments, from 300 to 250 K and from 150 to 100 K, with distinctly different electron/phonon-scattering amplitudes.

Based upon our measured VN room-temperature resistivity $\rho_{300\,\mathrm{K}}$, we estimate the conduction electron mean free path $\lambda_{300\,\mathrm{K}}$ via the relationship $\lambda_{300\,\mathrm{K}} = v_F(\varepsilon_o\omega_p^2\rho_{300\,\mathrm{K}})^{-1}$, in which ε_o is the permittivity of free space, v_F is the Fermi electron velocity, and ω_p is the unscreened plasma frequency. We obtain $\omega_p = 6.4\,\mathrm{eV}/\hbar$ from a Drude-Lorentz fit to the VN dielectric function obtained using variable-angle spectroscopic ellipsometry and confirmed by first-principles DFT band-structure calculations [15,74], which yield $\omega_p = 6.5\,\mathrm{eV}/\hbar$. Using the Fermi velocity $v_F = 2.09 \times 10^6\,\mathrm{m/s}$ [75,76] for NbN, which is isoelectronic with VN, yields $\lambda_{300\,\mathrm{K}} = 7\,\mathrm{nm}$, approximately $17\times$ the measured lattice parameter, $a_o = 0.4130\,\mathrm{nm}$. A linear extrapolation of $\rho(T)$ results near 300 K shows that $\lambda = a_o$ at $T \sim 10\,000\,\mathrm{K}$, greatly exceeding the VN melting point, $T_m = 2350\,\mathrm{K}$ [77]. Thus, we conclude that the

proposed sublinear decrease in $\rho(T)$ arising from a reduction in the electron mean free path to less than a_o does not occur.

The resistivity ρ_o of VN at temperatures $T \lesssim 20$ K remains constant at $2.12 \, \mu\Omega$ cm and is primarily determined by defect and impurity scattering. The presence of vacancies on both cation and anion VN sublattices exceeding a vacancy fraction of $f_{\text{vac}} \sim 0.06$ has been suggested to have a stabilizing effect on the NaCl structure [6]. An upper bound on the vacancy concentration in our VN films is obtained by comparing measured ρ_o values to those computed from first-principles electronic Green's function calculations using the Kubo-Greenwood formalism [29–34]. Self-consistent VN Green's functions are solved using the Korringa-Kohn-Rostoker approximation [37,38] as implemented in the simulations package SPR-KKR [32–34]. Electron scattering rates and perturbations to the periodic crystal potential arising from equal concentrations of cation and anion vacancies are modeled within the coherent-potential approximation [35]. Calculated low-temperature defect-controlled resistivities ρ_o increase linearly with vacancy fraction f_V following the empirical relationship $\rho_o(x) = 5.1 \times 10^2 \, f_{\text{vac}} \, \mu\Omega$ cm. Based on our measured ρ_o value, we establish an upper limit, $f_{\text{vac}} < 0.005$, to the vacancy fraction in our VN layers which is an order of magnitude smaller than the value $f_{\text{vac}} \sim 0.06$ predicted in Ref. [8] to influence the structural stability of VN. Thus, VN has the NaCl structure at room temperature despite having a much lower vacancy concentration.

For metallic conductors, the residual resistivity ratio RRR $= \rho_{300 \, \text{K}}/\rho_o$ serves as a metric for crystalline quality. Here, we obtain RRR $= 16$ for VN/MgO(011). Reported values for high-crystalline-quality group-IVB ZrN/MgO(001) layers are 15 [15], while previous studies of VN thin films yield RRR values of 8.4 [65] and 10 [67]. The relatively large RRR value obtained here reflects the stoichiometry and high structural quality of the present VN films. As a result, scattering events are independent and the temperature-dependent resistivity of the tetragonal-VN phase ($T < 250$ K) may be described by Matthiessen's rule: $\rho(T) = \rho_o + \rho_{\text{ph}}(T)$, in which $\rho_{\text{ph}}(T)$ is the phonon-scattering contribution to resistivity.

The VN resistivity between 100 and 10 K (Fig. 11) follows a power-law relationship $\rho_{\text{ph}}(T) \propto T^4$, which is characteristic of electron/phonon scattering in metals for which the Fermi surface intersects Bragg planes. This is in contrast to the normal $\rho_{\text{ph}}(T) \propto T^5$ behavior [78], when Umklapp processes dominate scattering [79,80] and electrons are frequently scattered outside of the first Brillouin zone [81]. The transport Eliashberg spectral function $\alpha_{\text{tr}}^2 F(\hbar\omega)$ [78] describes the effect of electron/phonon-scattering events on $\rho_{\text{ph}}(T)$ via the transform [82]:

$$\rho_{\text{ph}}(T) = \frac{\pi m^*}{ne^2} \int_0^\infty \frac{\hbar\omega/k_B T}{\sinh^2(\hbar\omega/2k_B T)} \alpha_{\text{tr}}^2 F(\hbar\omega) d\hbar\omega. \quad (2)$$

n, m^*, and e are the electron density, effective mass, and charge. By discretizing the integral in Eq. (2) into a series of Einstein modes at fixed energies, the scattering amplitude for each mode is adjusted through a least-squares procedure until the calculated $\rho_{\text{ph}}(T)$ result matches the measured curve. Based upon a collection of 1000 Einstein mode energies and corresponding amplitudes, obtained from approximately 100
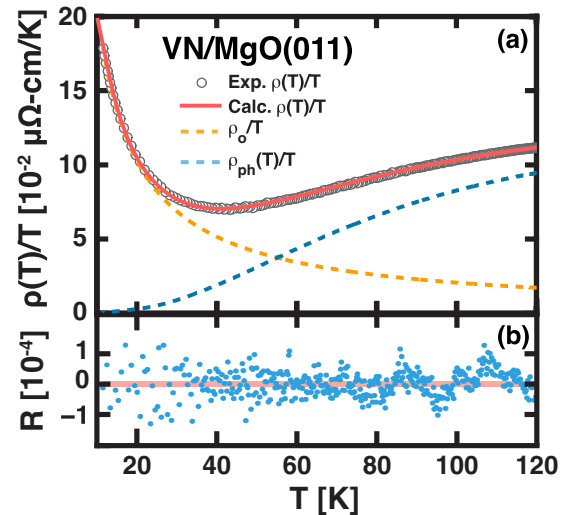
FIG. 12. (Color online) (a) Measured temperature-dependent resistivity $\rho(T)$ of epitaxial stoichiometric VN/MgO(011). $\rho(T)$ is multiplied by a factor of $1/T$ (circles) to highlight contributions due to defect scattering ρ_o (dashed orange line) and phonon scattering $\rho_{\text{ph}}(T)$ (dashed blue line). The solid red curve is the calculated total normalized VN resistivity $\rho(T)/T$, for which $\rho(T) = \rho_o + \rho_{\text{ph}}(T)$. (b) Residuals R, the difference between measured and calculated resistivities, as a function of temperature T.

fitting routines, a quasicontinuous Eliashberg spectral function describing electron/phonon coupling in the low-temperature tetragonal-VN phase is developed. A detailed account of the inversion procedure is presented in Ref. [15].

Figure 12 is a plot showing calculated VN temperature-dependent resistivities $\rho(T) = \rho_o + \rho_{\text{ph}}(T)$ between 125 and 10 K, multiplied by a factor $1/T$ (red solid line) to highlight resistivity contributions from defects (orange dashed curve) and phonon scattering (blue dashed curve). There is no discernible discrepancy between calculated $\rho(T)/T$ values and normalized experimental resistivity results (circles). Residuals R, defined as the difference between calculated and experimental curves, are plotted in Fig. 12(b) and show that the agreement is excellent, $R \leqslant 10^{-4}$, to within experimental uncertainty. These results establish that while electron/phonon scattering contributes essentially nothing to the VN resistivity below 20 K, it becomes the strongest electron scattering source above 57 K.

The transport VN Eliashberg spectral function $\alpha_{\text{tr}}^2 F(\hbar\omega)$ for the low-temperature tetragonal-VN phase is plotted in Fig. 13 for phonon energies $\hbar\omega$ between 0 and 60 meV. A strong contribution from electron/acoustic-phonon interactions gives rise to a peak at $\hbar\omega = 25$ meV. For comparison, measurements of phonon density of states $F(\hbar\omega)$ obtained from room-temperature inelastic neutron-scattering experiments carried out on bulk NaCl-structure VN reveal a softer acoustic-phonon peak at $\hbar\omega = 19$ meV [9]. The $F(\hbar\omega)$ shoulder at 30 meV arises from phonon van Hove singularities, i.e., regions in reciprocal space, including near the L-point Brillouin-zone boundary, for which the phonon group velocity $v_g = \nabla_k\omega$ is zero.

The Gibbs free energy of a dynamically stable, configurationally ordered, nonmagnetic, crystalline phase evolves with
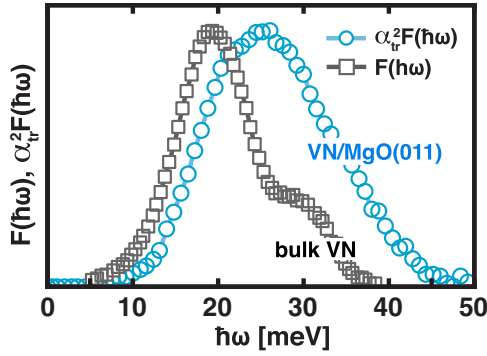
FIG. 13. (Color online) Acoustic contributions to the tetragonal-VN transport Eliashberg spectral function $\alpha_{tr}^2 F(\hbar\omega)$, obtained using an Einstein inversion procedure [15] from temperature-dependent ($10 < T < 125$ K) resistivity measurements of epitaxial stoichiometric VN/MgO(011) (blue circles). For comparison, room-temperature cubic-VN acoustic-phonon density of states $F(\hbar\omega)$ (gray squares), obtained from inelastic neutron-scattering measurements carried out with bulk samples [9].

temperature T as

$$G = G_o - T S_{\text{vib}} - T S_{\text{el}}, \tag{3}$$

in which S_{vib} and S_{el} are vibrational and electronic entropies and G_o is a temperature-independent factor which includes enthalpies and zero-point energies. The electronic entropy for VN is small ($\sim$1% of the vibrational entropy) and thus neglected. The vibrational entropy S_{vib}, for a dynamical stable phase, is given to leading order within anharmonic perturbation theory [83] by the Mermin functional as

$$
\begin{aligned}
&S_{\text{vib}}(T) \\
&= -\frac{\partial}{\partial T} \left\{ k_{\text{B}} T \int_0^\infty \ln\left[2\sinh\left(\frac{\hbar\omega}{2k_{\text{B}}T} \right) \right] F(\hbar\omega) d\hbar\omega \right\}_V
\end{aligned}
\tag{4}
$$

with the derivative evaluated at constant volume V. Consider Eq. (4) with an Einstein phonon density of states $F(\hbar\omega) = \delta(\hbar\omega^* - \hbar\omega)$, as would occur for a harmonic oscillator with a resonant energy $\hbar\omega^*$. In the limit of small $\hbar\omega^*$, the vibrational entropy simplifies to $S_{\text{vib}}(T) = k_{\text{B}}[1 - \ln(\hbar\omega^*) + \ln(k_{\text{B}}T) + \cdots]$, indicating that $S_{\text{vib}}(T)$ is higher for crystals with softer phonons, i.e., smaller $\hbar\omega^*$ values [84]. Physically, the higher entropy arises because smaller vibrational energies $\hbar\omega^*$ engender larger phonon populations which, in turn, yield more configurational microstates.

Comparing the inverted low-temperature tetragonal-VN transport Eliashberg spectral function $\alpha_{tr}^2 F(\hbar\omega)$, which gives rise to a peak at $\hbar\omega = 25$ meV (Fig. 13), and measured cubic-VN room-temperature neutron-scattering phonon densities of states $F(\hbar\omega)$, with a peak at $\hbar\omega = 19$ meV, we find that the entropy of the tetragonal phase $S_{\text{vib}}^{\text{tet}}$ is lower than that of the cubic phase $S_{\text{vib}}^{\text{cub}}$ over their respective temperature stability ranges. Additionally, the fact that VN adopts the tetragonal structure at low temperatures requires the enthalpy and zero-point vibrational energy [see Eq. (5)] of the tetragonal phase G_o^{tet} to be lower than that of the cubic phase G_o^{cub}. Thus, the relative Gibbs free energies of the tetragonal and cubic-VN

phases,

$$\Delta G \equiv \Delta G_o - T \Delta S_{\text{vib}}, \tag{5}$$

are related via

$$\Delta G_o \equiv G_o^{\text{tet}} - G_o^{\text{cub}} < 0, \tag{6}$$

and

$$\Delta S_{\text{vib}} \equiv S_{\text{vib}}^{\text{tet}} - S_{\text{vib}}^{\text{cub}} < 0. \tag{7}$$

The tetragonal phase is thermodynamically stable with respect to the cubic phase when $\Delta G < 0$ or, equivalently, when the temperature $T < T_c$; while the cubic phase is stable when $\Delta G > 0$ and $T > T_c$. At absolute zero, the temperature-independent free energy of the tetragonal phase is lower, rendering the cubic phase thermodynamically unstable. As T is raised over the range $0 < T < 250$ K, cubic VN remains dynamically unstable with imaginary phonon modes. At the critical phase-transition temperature $T_c = 250$ K, the difference in vibrational entropy $T \Delta S_{\text{vib}}$ balances the difference in the temperature-independent free energy ΔG_o. Additionally, anharmonic vibrations dynamically stabilize the cubic-VN phase so that all phonon energies become positive (see Fig. 10). At even higher temperatures, including at and above room temperature, the ground state of the VN system resides in the cubic phase, due to softer phonon modes and higher vibrational entropies of this state.

V. CONCLUSIONS

Single-crystal stoichiometric B1 NaCl-structure VN/MgO(011) layers grow with a cube-on-cube orientational relationship to the substrate: $(011)_{\text{VN}}||(011)_{\text{MgO}}$ and $[100]_{\text{VN}}||[100]_{\text{MgO}}$. At a critical transition temperature $T_c = 250$ K, temperature-dependent SAED and synchrotron XRD measurements reveal the presence of forbidden X-point reflections associated with a cubic-to-tetragonal phase transition. Upon further cooling, forbidden peak intensities I increase following the scaling behavior I $\propto (T_c - T)^{1/2}$.

Temperature-dependent VN/MgO(011) resistivities decrease from $\rho_{300\,\text{K}} = 33.0\,\mu\Omega\,\text{cm}$ ($T = 300$ K) to $\rho_o = 2.12\,\mu\Omega\,\text{cm}$ ($T \lesssim 20$ K). Both the room-temperature $\rho_{300\,\text{K}}$ and residual ρ_o resistivity results are the lowest reported values for bulk and thin film VN, reflecting the high structural quality of our films. VN resistivities $\rho(T)$ over the temperature range from 300 to 100 K contain two linear regions for which TCR values are $17 \times 10^{-8}\,\Omega\,\text{cm}\,\text{K}^{-1}$ ($250 \lesssim T \lesssim 300$ K) and $6.4 \times 10^{-8}\,\Omega\,\text{cm}\,\text{K}^{-1}$ ($100 \lesssim T \lesssim 150$ K). Smaller TCR values at higher temperatures were previously believed to be the result of electron/phonon scattering reducing VN conduction electron mean free paths λ to lengths comparable to interatomic distances [72,85]. However, we find that $\lambda = a_o$, the relaxed VN lattice parameter, only for temperatures greatly exceeding the VN melting point. Instead, we interpret the change in TCR as arising from the cubic-to-tetragonal phase transition at 250 K.

AIMD simulations based on the TDEP method reveal that lattice vibrations in NaCl-structure VN are strongly anharmonic. An analysis of temperature-dependent renormalized VN phonon dispersion relations shows that VN is dynamically unstable in the NaCl structure below $T_c = 250$ K resulting in unphysical X-point longitudinal acoustic-phonon energies

($\hbar\omega_{LA}^2 < 0$). However, above this temperature, the NaCl structure is stabilized by anharmonic effects. Transport Eliashberg spectral function results, obtained from temperature-dependent resistivity measurements, combined with anharmonic perturbation theory, establish that NaCl-structure VN is thermodynamically stabilized at $T > T_c$ relative to the tetragonal-VN phase due to lower phonon energies and, consequentially, higher vibrational entropies.

[1] H. Yusa, F. Kawamura, T. Taniguchi, N. Hirao, Y. Ohishi, and T. Kikegawa, J. Appl. Phys. **115**, 103520 (2014).

[2] C.-S. Shin, Y.-W. Kim, D. Gall, J. E. Greene, and I. Petrov, Thin Solid Films **402**, 172 (2002).

[3] S.-J. Kim and H. F. Franzen, J. Less-Common Met. **143**, 339 (1988).

[4] A. I. Gusev, Phys. Status Solidi B **209**, 267 (1998).

[5] E. I. Isaev, S. I. Simak, I. A. Abrikosov, R. Ahuja, Y. K. Vekilov, M. I. Katsnelson, A. I. Lichtenstein, and B. Johansson, J. Appl. Phys. **101**, 123519 (2007).

[6] V. I. Ivashchenko and P. E. A. Turchi, Phys. Rev. B **78**, 224113 (2008).

[7] F. Kubel, W. Lengauer, K. Yvon, K. Knorr, and A. Junod, Phys. Rev. B **38**, 12908 (1988).

[8] V. I. Ivashchenko, P. E. A. Turchi, V. I. Shevchenko, and E. I. Olifan, Phys. Rev. B **84**, 174108 (2011).

[9] W. Weber, P. Roedhammer, L. Pintschovius, W. Reichardt, F. Gompf, and A. N. Christensen, Phys. Rev. Lett. **43**, 868 (1979).

[10] A. B. Mei, R. B. Wilson, D. Li, D. G. Cahill, A. Rockett, J. Birch, L. Hultman, J. E. Greene, and I. Petrov, J. Appl. Phys. **115**, 214908 (2014).

[11] D. C. Wallace, *Thermodynamics of Crystals* (Courier Dover Publications, Mineola, NY, 1998).

[12] A. Thore, M. Dahlqvist, B. Alling, and J. Rosén, Comput. Mater. Sci. **91**, 251 (2014).

[13] O. Hellman, P. Steneteg, I. A. Abrikosov, and S. I. Simak, Phys. Rev. B **87**, 104111 (2013).

[14] O. Hellman, I. A. Abrikosov, and S. I. Simak, Phys. Rev. B **84**, 180301 (2011).

[15] A. B. Mei, A. Rockett, L. Hultman, I. Petrov, and J. E. Greene, J. Appl. Phys. **114**, 193708 (2013).

[16] I. Petrov, F. Adibi, J. E. Greene, W. D. Sproul, and W.-D. Munz, J. Vac. Sci. Technol., A **10**, 3283 (1992).

[17] R. C. Powell, N.-E. Lee, Y.-W. Kim, and J. E. Greene, J. Appl. Phys. **73**, 189 (1993).

[18] M. Mayer, Nucl. Instrum. Methods B **332**, 176 (2014).

[19] L. J. van der Pauw, Philips Res. Repts. **13**, 1 (1958).

[20] R. P. Feynman, Phys. Rev. **56**, 340 (1939).

[21] H. Hellmann, *Einführung in die Quantenchemie* (Franz Deuticke, Vienna, Austria, 1937).

[22] W. Kohn and L. J. Sham, Phys. Rev. **140**, A1133 (1965).

[23] P. E. Blöchl, Phys. Rev. B **50**, 17953 (1994).

[24] G. Kresse and J. Hafner, Phys. Rev. B **48**, 13115 (1993).

[25] G. Kresse and D. Joubert, Phys. Rev. B **59**, 1758 (1999).

[26] G. Kresse and J. Furthmüller, Phys. Rev. B **54**, 11169 (1996).

[27] R. Armiento and A. E. Mattsson, Phys. Rev. B **72**, 085108 (2005).

[28] S. Nosé, Mol. Phys. **52**, 255 (1984).

[29] R. Kubo, J. Phys. Soc. Jpn. **12**, 570 (1957).

[30] W. H. Butler, Phys. Rev. B **31**, 3260 (1985).

[31] D. A. Greenwood, Proc. Phys. Soc. **71**, 585 (1958).

[32] H. Ebert, A. Vernes, and J. Banhart, Phys. Rev. B **54**, 8479 (1996).

[33] H. Ebert, in *Electronic Structure and Physical Properies of Solids*, edited by P. H. Dreyssé (Springer Berlin, Heidelberg, Germany, 2000), pp. 191–246.

[34] H. Ebert, D. Ködderitzsch, and J. Minár, Rep. Prog. Phys. **74**, 096501 (2011).

[35] J. S. Faulkner and G. M. Stocks, Phys. Rev. B **21**, 3222 (1980).

[36] In addition to the two atomic spheres located at the 0,0,0 and ½,½,½ atomic sites of the NaCl cell, two empty spheres with equivalent radii are centered about ¼,¼,¼ and −¼,−¼,−¼. The additional spheres are required to extend the basis over which the electronic wave functions can be expanded into their spherical harmonics; using the additional spheres, we obtain an electronic band structure which is in excellent agreement with that obtained from VASP. Without the empty spheres, the band structure exhibits artifacts which arise from not properly describing the electronic wave functions.

[37] J. Korringa, Physica **13**, 392 (1947).

[38] W. Kohn and N. Rostoker, Phys. Rev. **94**, 1111 (1954).

[39] J. P. Perdew, K. Burke, and M. Ernzerhof, Phys. Rev. Lett. **77**, 3865 (1996).

[40] H. O. Pierson, *Handbook of Refractory Carbides and Nitrides: Properties, Characteristics, Processing and Applications*, 1st ed. (William Andrew, Westwood, NJ, 1997).

[41] P. van der Sluis, J. Phys. D Appl. Phys. **26**, A188 (1993).

[42] C.-S. Shin, S. Rudenja, D. Gall, N. Hellgren, T.-Y. Lee, I. Petrov, and J. E. Greene, J. Appl. Phys. **95**, 356 (2004).

[43] A. B. Mei, B. M. Howe, C. Zhang, M. Sardela, J. N. Eckstein, L. Hultman, A. Rockett, I. Petrov, and J. E. Greene, J. Vac. Sci. Technol., A **31**, 061516 (2013).

[44] D. K. Bowen and B. K. Tanner, *High Resolution X-Ray Diffractometry and Topography* (CRC Press, Bristol, PA, 1998).

[45] H. Hahn, Z. Anorg. Chem. **258**, 58 (1949).

[46] L. Toth, C. Wang, and G. Yen, Acta Metall. **14**, 1403 (1966).

[47] H. Holleck, J. Vac. Sci. Technol., A **4**, 2661 (1986).

[48] W. Lengauer and P. Ettmayer, Monatsh. Chem. **117**, 713 (1986).

[49] X. Y. Zhang, J. S. Chawla, R. P. Deng, and D. Gall, Phys. Rev. B **84**, 073101 (2011).

[50] L. D. Landau and E. M. Lifshitz, *Statistical Physics, Third Edition, Part 1*, Course of Theoretical Physics Vol. 5 (Butterworth-Heinemann, Kidlington, England, 1980).

[51] R. Xu and T.-C. Chiang, Phase Transitions **83**, 99 (2010).

[52] R. Xu, J. Wong, P. Zschack, H. Hong, and T.-C. Chiang, Europhys. Lett. **82**, 26001 (2008).

[53] G. Shirane, J. D. Axe, J. Harada, and J. P. Remeika, Phys. Rev. B **2**, 155 (1970).

[54] G. Grimvall, B. Magyari-Köpe, V. Ozoliņš, and K. A. Persson, Rev. Mod. Phys. **84**, 945 (2012).

[55] A. N. Christensen, O. W. Dietrich, W. Kress, W. D. Teuchert, and R. Currat, Solid State Commun. **31**, 795 (1979).

[56] X.-J. Chen, V. V. Struzhkin, S. Kung, H.-K. Mao, R. J. Hemley, and A. N. Christensen, Phys. Rev. B **70**, 014501 (2004).

[57] K.-P. Bohnen, R. Heid, and B. Renker, Phys. Rev. Lett. **86**, 5771 (2001).

[58] M. d'Astuto, M. Calandra, S. Reich, A. Shukla, M. Lazzeri, F. Mauri, J. Karpinski, N. D. Zhigadlo, A. Bossak, and M. Krisch, Phys. Rev. B **75**, 174508 (2007).

[59] P. Zhang, Y. Xue, and P. Dev, Solid State Commun. **148**, 151 (2008).

[60] M. Monni, I. Pallecchi, C. Ferdeghini, V. Ferrando, A. Floris, E. G. d'Agliano, E. Lehmann, I. Sheikin, C. Tarantini, X. X. Xi, S. Massidda, and M. Putti, Europhys. Lett. **81**, 67006 (2008).

[61] A. Y. Liu, I. I. Mazin, and J. Kortus, Phys. Rev. Lett. **87**, 087005 (2001).

[62] Y. Kong, O. V. Dolgov, O. Jepsen, and O. K. Andersen, Phys. Rev. B **64**, 020501 (2001).

[63] A. G. Zaitsev, R. Schneider, O. de la Pe–a-Seaman, R. de Coss, R. Heid, K.-P. Bohnen, and J. Geerk, Phys. Procedia **36**, 479 (2012).

[64] M. B. Takeyama, T. Itoi, K. Satoh, M. Sakagami, and A. Noya, J. Vac. Sci. Technol., B **22**, 2542 (2004).

[65] J. F. Zasadzinski, A. Saggese, K. E. Gray, R. T. Kampwirth, and R. Vaglio, Phys. Rev. B **38**, 5065 (1988).

[66] B. R. Zhao, L. Chen, H. L. Luo, M. D. Jack, and D. P. Mullin, Phys. Rev. B **29**, 6198 (1984).

[67] N. Tralshawala, J. F. Zasadzinski, L. Coffey, W. Gai, M. Romalis, Q. Huang, R. Vaglio, and K. E. Gray, Phys. Rev. B **51**, 3812 (1995).

[68] H. S. Seo, T. Y. Lee, J. G. Wen, I. Petrov, J. E. Greene, and D. Gall, J. Appl. Phys. **96**, 878 (2004).

[69] A. Cassinese, M. Iavarone, R. Vaglio, M. Grimsditch, and S. Uran, Phys. Rev. B **62**, 13915 (2000).

[70] F. Nava, O. Bisi, and K. N. Tu, Phys. Rev. B **34**, 6143 (1986).

[71] M. Gurvitch, A. K. Ghosh, H. Lutz, and M. Strongin, Phys. Rev. B **22**, 128 (1980).

[72] M. Gurvitch, Phys. Rev. B **24**, 7404 (1981).

[73] O. Gunnarsson, M. Calandra, and J. E. Han, Rev. Mod. Phys. **75**, 1085 (2003).

[74] G. K. H. Madsen and D. J. Singh, Computer Phys. Commun. **175**, 67 (2006).

[75] S. P. Chockalingam, M. Chand, J. Jesudasan, V. Tripathi, and P. Raychaudhuri, Phys. Rev. B **77**, 214503 (2008).

[76] M. Mondal, A. Kamlapure, S. C. Ganguli, J. Jesudasan, V. Bagwe, L. Benfatto, and P. Raychaudhuri, Sci. Rep. **3**, 1 (2013).

[77] D. L. Perry, *Handbook of Inorganic Compounds*, 2nd ed. (Taylor & Francis US, Boca Raton, FL, 2011).

[78] G. Grimvall, *The Electron-Phonon Interaction in Metals* (North-Holland Pub. Co.: Sole distributors for the USA and Canada; Elsevier North-Holland, Amsterdam; New York, NY, 1981).

[79] J. Ekin, *Experimental Techniques for Low-Temperature Measurements: Cryostat Design, Material Properties and Superconductor Critical-Current Testing* (Oxford University Press, London, England, 2006).

[80] W. E. Lawrence and J. W. Wilkins, Phys. Rev. B **6**, 4466 (1972).

[81] A. H. MacDonald, R. Taylor, and D. J. W. Geldart, Phys. Rev. B **23**, 2718 (1981).

[82] G. v. Minnigerode, Berich. Bunsen Gesell. **87**, 453 (1983).

[83] W. Cochran and R. A. Cowley, in *Light and Matter Ia/Licht Und Materie Ia*, edited by L. Genzel (Springer, Berlin, Heidelberg, Germany, 1967), pp. 59–156.

[84] Unstable phases do not appear in the equilibrium phase diagram, since their vibrational entropy is undefined. As a soft-mode phase transition is approached, the phonon energies of the dynamically stable phase approach zero, increasing the vibrational entropy of the system. Since the energy of the unstable phonon branch varies parabolically near the point of instability, the density of states $F(\hbar\omega)$ suppresses the logarithmic divergence in Eq. (4) yielding an entropy which is finite and slowly varying as a function of temperature [54,86]. Thus, the excess entropy associated with the vibrational instability can be modeled using a smooth interpolation from the region where the corresponding phase is dynamically (and thermodynamically) stable [87].

[85] N. E. Hussey, K. Takenaka, and H. Takagi, Philos. Mag. **84**, 2847 (2004).

[86] A. Fernández Guillermet, V. Ozoliņš, G. Grimvall, and M. Körling, Phys. Rev. B **51**, 10364 (1995).

[87] P. E. A. Turchi, V. Drchal, J. Kudrnovský, C. Colinet, L. Kaufman, and Z.-K. Liu, Phys. Rev. B **71**, 094206 (2005).